International Journal of Solids and Structures 322 (2025) 113633

Contents lists available at ScienceDirect

International Journal of Solids and Structures

journal homepage: www.elsevier.com/locate/ijsolstr

Fretting fatigue crack initiation behaviour of Ti-6Al-4V and IN-100 alloys at elevated temperatures

Bilal Ahmed [a], Can Wang [a], Dagang Wang [b], Yunlai Zhou [c], Lihua Wang [d,*], Magd Abdel Wahab [a,d,e,*]

[a] Soete Laboratory, Department of Electrical Energy, Metals, Mechanical Constructions, and Systems, Faculty of Engineering and Architecture, Ghent University, Belgium
[b] School of Mechanical and Electrical Engineering, China University of Mining and Technology, Xuzhou 221116, China
[c] State Key Laboratory for Strength and Vibration of Mechanical Structures, School of Aerospace Engineering, Xi'an Jiaotong University, China
[d] School of Aerospace Engineering and Applied Mechanics, Tongji University, Shanghai 200092, China
[e] Parallel and Distributed Systems Laboratory, Jožef Stefan Institute, Jamova cesta 39, Ljubljana SI-1000, Slovenija

ARTICLE INFO

Keywords:
Fretting fatigue
High temperatures
Critical plane method
Crack initiation

ABSTRACT

Fretting fatigue is a critical concern in high temperature applications. This study presents a numerical investigation of fretting fatigue crack initiation behaviour of Ti-6Al-4 V and IN-100 alloys at elevated temperatures. Three multiaxial fatigue damage parameters are considered, namely the stress-based Findley Parameter (FP), the strain-based Fatemi–Socie (FS) parameter, and the strain energy-based Smith–Watson–Topper (SWT) parameter. A new zone-based method is proposed to estimate crack initiation parameters, based on subsurface stress averaging across discretized angular zones beneath the contact surface. The numerical predictions are validated against experimental data from the literature. FS and SWT parameters demonstrate improved predictive capability under elevated temperatures due to their ability to capture the effect of thermal strains. In contrast, FP, being purely stress-based, does not account for the strains and thus exhibits reduced accuracy at high temperatures. The zone-based method shows improved accuracy for crack orientation.

1. Introduction

Fretting is caused when contact surfaces are exposed to vibration, cyclic strain or fatigue loading and a small-amplitude oscillatory tangential movement. Normal load, slip amplitude, and frequency are examples of contact parameters that influence the extent of surface damage resulting from fretting fatigue. The alternating loads in the contact area are the source of early initiation of small fatigue cracks leading to fatigue failures (Waterhouse, 1981). Relative displacements combined with tensile and shear stresses can cause oxidation, wear, and crack initiation resulting in significant reduction in fatigue lives of materials and components (Li et al., 1999).

In aviation sector, an aero-engine's compressor is essential component for both compressing and boosting air. The compressor's operating temperature may reach 600 °C, and its blades must withstand high rotation speeds in addition to severe pressure and temperature environments. Fretting fatigue is a commonly observed damage mechanism in aircraft turbine shafts and dovetail blade attachments (Golden and Naboulsi, 2012; Yang, 2019; Mangardich et al., 2019; Su, 2019; Chen, 2019). During the operation of aircraft engine, micrometre-scale sliding between the surfaces causes fretting wear in the contact areas. Surface damage from wear eventually results in stress concentrations in weak areas, which eventually turn into microcracks. These cracks may lead to a fatigue fracture at the blade root as they deepen. Fretting fatigue is a major worry in the blade-disk connection since it is a typical cause of engine blade failures and has been connected to multiple aviation crashes (Nikitin et al., 2023; Shi, 2017; Sujata, 2013; Kuang, 2022). High-strength materials such as titanium alloys or nickel-based superalloys are generally used in manufacturing these blades.

Experimental and numerical research on the impact of wear on the nickel-based alloy's fretting fatigue behaviour at higher temperatures was conducted by Almeida et al. (Almeida, 2023). Smith Watson Topper (SWT) parameter was used in conjunction with critical distance technique to predict total life regarding and disregarding wear. Wang et al. (Wang, 2024) implemented numerical simulations to analyse how different surface conditions affect the initiation orientation and paths of GH4169 super-alloy at 650 °C. Mall et al. (Mall, 2010) investigated the

* Corresponding authors at: Soete Laboratory, Department of Electrical Energy, Metals, Mechanical Constructions, and Systems, Faculty of Engineering and Architecture, Ghent University, Belgium.
E-mail addresses: lhwang@tongji.edu.cn (L. Wang), Magd.abdelwahab@UGent.be (M. Abdel Wahab).

https://doi.org/10.1016/j.ijsolstr.2025.113633
Received 18 June 2025; Received in revised form 20 August 2025; Accepted 25 August 2025
Available online 26 August 2025

Nomenclature

σ_{axial}	Applied axial stress
$\sigma_{axial,max}$	Maximum axial stress
$\sigma_{axial,min}$	Minimum axial stress
$\sigma_{Reaction}$	Reaction stress
Q	Tangential load
Q_{max}	Maximum tangential load
Q_{min}	Minimum tangential load
p_{max}	Maximum normal pressure at contact
$p(x)$	Pressure distribution at contact surface
$q(x)$	Shear stress distribution at contact surface
a	Half contact width
$\frac{\Delta\tau_{max}}{2}$	Maximum shear stress amplitude
$\frac{\Delta\varepsilon_1}{2}$	Principal strain amplitude
σ_n^{max}	Maximum normal stress
$\frac{\Delta\varepsilon_n}{2}$	Normal strain amplitude
k	Material constant
N_i	Number of cycles to crack initiation
N_f	Number of cycles to failure
τ_f'	Shear fatigue strength coefficient
b'	Fatigue exponent in torsion
b	Fatigue exponent in tension
c	Fatigue ductility exponent
σ_f'	Tensile fatigue strength coefficient
ε_f'	Fatigue ductility coefficient
σ_f	Plain specimen fatigue strength
σ_y	Yield stress
c_o	Stick zone boundary
l_c	Critical radius
ΔK_{th}	Threshold stress intensity factor range
θ	Crack initiation angle
μ	Coefficient of friction
R	Radius of the pad
T	Temperature
CTE	Coefficient of thermal expansion
E	Modulus of elasticity
ν	Poisson's ratio
A	Cross section area of specimen
F	Normal load

influence of contact load and grain size on the fretting fatigue and plain fatigue behaviour of IN-100 at 600 °C. Their findings highlighted the sensitivity of fatigue life to both mechanical loading conditions and microstructural features. Ownby (Ownby, 2008) conducted an experimental investigation on the fretting fatigue behaviour of IN-100 at 600 °C and reported an improvement in fretting fatigue life due to the formation of an oxide layer. The oxide layer was found to act as a protective barrier, reducing the severity of metal-to-metal contact and mitigating surface damage, thereby extending the crack initiation life under fretting conditions. Many other researchers have numerically studied the behaviour of nickel-based alloys at high temperature (Sun, 2024; Qu, 2021; Zhai, 2020; Sunde et al., 2021; Yuan, 2023). Sahan et al. (Sahan, 2002) investigated both numerically and experimentally the crack initiation, orientation and location of Ti-6Al-4 V at increased temperature (260 °C). Maximum value of Critical Plane (CP) parameters was used for fretting fatigue and plain fatigue both at room and high temperatures. Due to free end boundary condition, the temperature effect in numerical model was incorporated by using material properties at high temperature without applying temperature loads. In another work (Jin et al., 2005), the authors employed modified shear stress range parameter to study crack initiation behaviour under fretting fatigue and observed that the Coefficient of Friction (CoF) increased marginally before stabilizing at a constant level of 260 °C. Albinali (Albinali, 2005) investigated the effect of surface hardening treatments at high temperature and fretting fatigue life was correlated with the plain fatigue life.

Several experimental investigations and numerical results have demonstrated that the surface layer's contact zone has a multi-axial stress condition (Hu, 2019). As a result, fretting fatigue analysis has successfully employed CP techniques in conjunction with numerical analysis results. These methodologies focus on calculating CP parameters on planes having the highest probability of failure (Bhatti and Wahab, 2018). While using CP parameters to determine crack initiation angles, numerical models more often predicted the dominating crack orientation extending out of the contact ($+\theta$) (Bhatti and Wahab, 2017; Lykins et al., 2001; Lykins et al., 2000; Naboulsi and Mall, 2003; Li et al., 2015; Pereira et al., 2018) whereas, the majority of the experimental data demonstrated the orientation of fracture initiation within the contact region ($-\theta$) (Szolwinski and Farris, 1998; Goh, 2001; Proudhon et al., 2005; Hojjati-Talemi, 2014; Walvekar, 2014). Bhatti et al. (Bhatti et al., 2019) proposed a quadrant averaging method capable of incorporating high stress gradient and compared the results with conventional point and volume averaging method. More accurate results for the orientation of crack initiation were obtained with the suggested method.

In this study, a numerical model is developed to investigate the

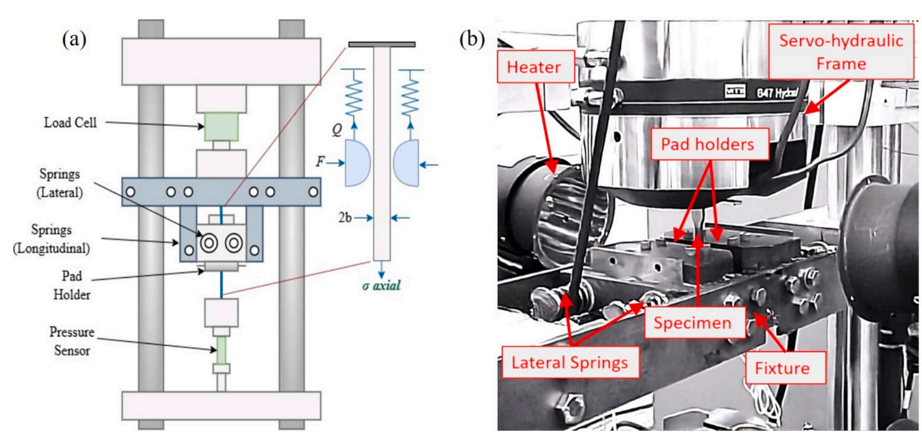

Fig. 1. Fretting fatigue experimental setup: (a) schematic diagram and (b) test setup (Ownby, 2008; Sahan, 2002).

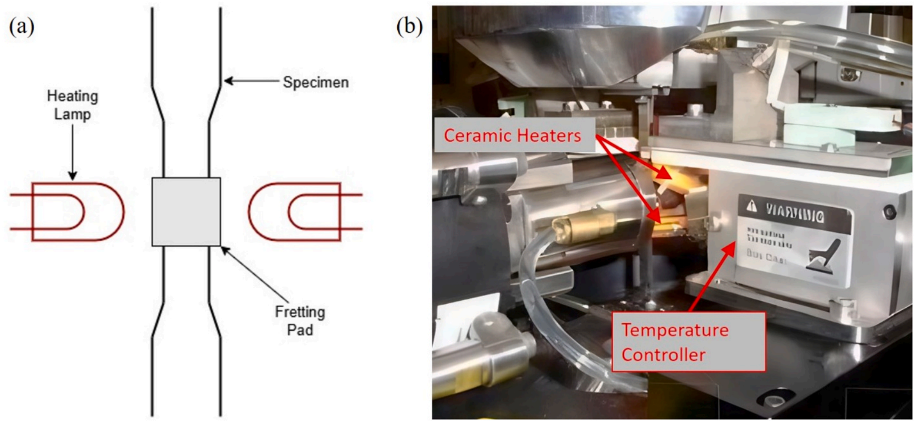

Fig. 2. Heating sources to maintain temperature: (a) infrared lamps and (b) ceramic heaters (Ownby, 2008; Sahan, 2002).

Table 1
Experimental dataset for Ti-6Al-4 V alloy (Sahan, 2002).

Test Number	$\sigma_{axial,max}$ (MPa)	$\sigma_{axial,min}$ (MPa)	Q_{max} (N)	Q_{min} (N)	N_f (cycles)
1	554	73.91	585	−220	77,732
2	503.6	68.766	470	−165	261,755
3	439.25	81.269	470	−89	244,338
4	506.18	95.97	483	−177	152,341
5	401.2	70.97	720	60	316,513
6	362.21	53.321	505	−90	3,338,962

fretting fatigue crack initiation behaviour at elevated temperatures. The model is constructed and validated using two materials: Ti-6Al-4 V alloy tested at 260 °C and IN-100 alloy tested at 600 °C. A detailed analysis is carried out to examine the influence of elevated temperature on fretting contact conditions and the evolution of multiaxial critical plane fatigue parameters. A new approach based on a modified line method is proposed for estimating crack orientation.

2. Material and experiments

The experimental dataset used to construct numerical model in this study is taken from the literature focussing on Ti-6Al-4 V alloy at 260 °C (Sahan, 2002) and IN-100 alloy 600 °C (Ownby, 2008) belonging to titanium and nickel families, respectively. Contact configuration in both cases was a cylinder on flat as shown in Fig. 1 with pad and test specimen geometries being cylindrical and flat, respectively. The cylindrical pads were 50.8 mm in radius, while the specimen thickness, 2b = 3.81 mm and, width, w = 6.35 mm. The desired test temperatures in both cases were achieved and maintained through the use of external heating sources as shown in Fig. 2. Details for each case are provided in the following sections.

2.1. Case 1: Ti-6Al-4 V alloy

A fretting fixture was constructed using a 100 kN servo-hydraulic test frame that would hold two fretting pads up against the specimen's faces as shown in Fig. 1(b) (Sahan, 2002). An extra 22 kN load cell was attached on the actuator to track tangential, or frictional force. This setup enabled the measurement of tangential forces on the cylindrical pad, determined as half of the difference between the load cell measurements. The fretting pads were subjected to a normal load of 1334 N. At a frequency of 10 Hz, fretting fatigue tests under a constant amplitude were conducted both at room temperature and at 260 °C, covering a range of applied stresses amplitudes. To determine the coefficient of friction, some displacement-controlled experiments were conducted in ref. (Sahan, 2002). In these experiments, the axial load was gradually increased until it stabilized. This constant axial force was considered to represent the frictional force. By dividing this value by the applied normal load, the coefficient of friction was calculated. The measurements were initially done without cycling the specimen, and subsequently after 5000 and 10,000 loading cycles at elevated temperature. It was observed that the coefficient of friction stabilized after approximately 10,000 cycles. The stabilized coefficient of friction was 0.55. The test temperature was maintained within a range of ± 5 °C throughout the experiments. Two infrared lamps were placed on both sides of the test specimen, as indicated in Fig. 1(b), in order to achieve and regulate the desired temperature. Table 1 lists the experimental dataset that was used in this study. The axial loads were applied and varied using the servohydraulic load frame, with load cells attached to monitor and control the axial stress throughout the fretting fatigue tests. The axial stress values in the Table 1 are the actual measured values, which deviate from the intended stress ratio of $R = 0.1$. These measured axial stress values are used in the present study to reflect the actual experimental conditions.

2.2. Case 2: IN-100 alloy

The experimental data for this case is taken from Ref. (Ownby, 2008). The material employed in this investigation was IN-100 alloy, a nickel-based superalloy fabricated via powder metallurgy. Fatigue testing was carried out using a servo-hydraulic testing machine integrated with a fretting apparatus. The configuration of the fretting system was same as illustrated schematically in Fig. 1(a). A hydraulic ram mounted on a movable sled applied a normal contact force, P, to both lateral faces of the specimen via a pair of loading pads, with load monitoring achieved through an integrated load cell. Two ceramic heating elements (Crystal® igniter Model 271) were mounted within heater boxes positioned symmetrically on both sides of the specimen, each inclined at approximately 30° from horizontal (Fig. 2(b)). These heater boxes were secured via screws through adjustable channels to a sled that also held the fretting actuator, allowing precise positioning without direct contact between the elements, specimen, and fretting pads. Thermocouples attached to the heater boxes maintained consistent relative positions to the specimen, heating elements, and fretting pads across all tests. A calibration process was performed before actual testing. A dummy specimen, identical in geometry to the test specimens, was instrumented with thermocouples spot-welded near the contact pads. Using this setup, a temperature profile was established by correlating the readings from the specimen-mounted thermocouples with those on the heater boxes, where thermocouples were permanently installed. This allowed for the creation of calibration curves which were then used to maintain and verify consistent temperature during actual tests. As a result, testing temperature of 600 °C was maintained

Table 2
Experimental dataset for IN-100 alloy (Ownby, 2008).

Test Number	$\sigma_{axial,max}$(MPa)	$\sigma_{axial,min}$(MPa)	Q_{max} (N)	Q_{min} (N)	N_f (cycles)
1	650	122.50	1099.58	332.63	2,464,530
2	800	24	698.14	1.06	170,160
3	750	22.5	994.75	153.46	1,326,201
4	850	25.5	1038.49	186.79	353,127
5	950	28.5	876.64	−240.83	60,232
6	650	19.5	1021.88	141.39	5,565,917
7	950	28.5	600.05	−409.44	71,951

consistently along the 12 mm gauge section, with a variation margin of ± 6 °C. Fretting fatigue experiments were conducted under tension–tension cyclic loading, with maximum axial stress levels varying between 650 MPa and 950 MPa. All tests were performed at a frequency of 10 Hz.

During the fretting tests, the pads exerted a constant normal contact force of 4003 N applied to the specimen's side surfaces. These pads also induced tangential forces (Q), which were calculated based on load measurements recorded independently on each side of the specimen. All fretting fatigue experiments were characterized by partial slip conditions, which were confirmed through analysis of the hysteresis loops correlating axial load and tangential force. Table 2 presents the stabilized stress and load values used to construct numerical model in this study (Ownby, 2008).

The coefficient of friction for our numerical model is adopted from Ref. (Mall, 2010), which tested the same material under a 4000 N normal load at 600 °C. In those experiments, Q/P rose from 0.15 to 0.25 during the first 100–500 cycles to a stabilized 0.30–0.40. Since Q/P = 0.4 corresponds to the effective friction limit (Q = μP) just before gross sliding and reflects the steady partial-slip condition, the coefficient of friction in the present study is taken as 0.4.

3. Theoretical Background

3.1. Hertz contact mechanics

The Hertz contact mechanics is presented in this section to provide the analytical solution for cylinder-plane contact interfaces as shown in the experimental setup in section 2. The contact stress and shear traction profiles are commonly determined using the Hertz theory. The theory is used under the presumptions that the strains are under the elastic limit, the contact is frictionless, and the contact area is substantially less than the dimension of the test specimen. It is believed that the surfaces in contact are non-conforming and continuous. Eq. (1) is used to express the maximum normal contact stress:

$$p_{max} = \sqrt{\frac{FE'}{t\pi R'}} \tag{1}$$

where F is the normal force, R' is the equivalent radius, t is the pad and specimen thickness and E' is the equivalent elastic modulus. R' is given by:

$$\frac{1}{R'} = \frac{1}{R_1} + \frac{1}{R_2} \tag{2}$$

where R_1 and R_2 represent the radii of two cylinders. Eq. (3) is used to calculate the equivalent modulus of elasticity:

$$\frac{1}{E'} = \frac{1-\nu_1^2}{E_1} + \frac{1-\nu_2^2}{E_2} \tag{3}$$

where ν_1 and ν_2 are Poisson's ratios, E_1 and E_2 are moduli of elasticity for the cylinders and test specimen, respectively. In terms of geometrical parameters and applied normal load, contact half width a is expressed as:

$$a = 2\sqrt{\frac{FR'}{t\pi E'}} \tag{4}$$

Then, the resulting pressure distribution at the contact surface in terms of peak normal contact stress is found using Eq. (5):

$$p(x) = -p_{max}\sqrt{1-\left(\frac{x}{a}\right)^2} \tag{5}$$

However, when fretting occurs, there is a friction force Q in tangential direction in addition to the normal applied force F. Studies (Williams and Dwyer-Joyce, 2001) have shown that in the absence of tangential forces, the pressure distribution $p(x)$ is unchanged. It is possible to simulate the shear stress profile on the contact surface $q(x)$ using $p(x)$ and CoF. On the contact surface, a stick and a slip zone are formed when $Q < \mu F$, with c denoting the stick zone's half-width. The Mindlin analytical solution is used for the two cylinders being subjected to forces F and Q, respectively with $Q < \mu F$ (Mindlin, 1949; Mindlin and Deresiewicz, 1953). Following that, Eq. (6) defines $q(x)$ as:

$$q(x) = \begin{cases} -p_{max}\mu\sqrt{1-\left(\frac{x}{a}\right)^2} & \text{if } c_o \le |x| \le a \\ -p_{max}\mu\left[\sqrt{1-\left(\frac{x}{a}\right)^2} - \frac{c}{a}\sqrt{1-\left(\frac{x}{c_o}\right)^2}\right] & \text{if } |x| < c_o \end{cases} \tag{6}$$

where

$\frac{c_o}{a} = \sqrt{1-\frac{Q}{\mu F}}$ (7) In the context of the present study, one side of the flat specimen is subject to an axial bulk stress σ_{axial} as indicated in Section 2. As a result, the effect of bulk stress must be incorporated with $q(x)$. Eq. (8) presents the updated $q(x)$ (Nowell et al., 2006):

$$\text{q}(x) = \begin{cases} -p_{max}\mu\sqrt{1-\left(\frac{x}{a}\right)^2} & \text{if } c_o \le |x| \le a \\ -p_{max}\mu\left[\sqrt{1-\left(\frac{x}{a}\right)^2} - \frac{c_o}{a}\sqrt{1-\left(\frac{x-e}{c_o}\right)^2}\right] & \text{if } |x+e| < c_o \end{cases} \tag{8}$$

where

$$e = a\frac{\sigma_{\text{axial}}}{4\mu p_{max}} \tag{9}$$

3.2. Critical Plane (CP) approaches

The CP approach is grounded on the idea that the material failure arises from damage accumulating on certain planes where cracks originate and propagate. Such planes are normal to the plane where maximum principal stress resides or close to the planes where shear stress is maximum. Findley (Findley et al., 1956; Findley, 1959) initially introduced the critical plane concept in the 1950 s for addressing uniaxial fatigue problems. Since then, various multiaxial fatigue damage parameters have been developed, generally classified into three

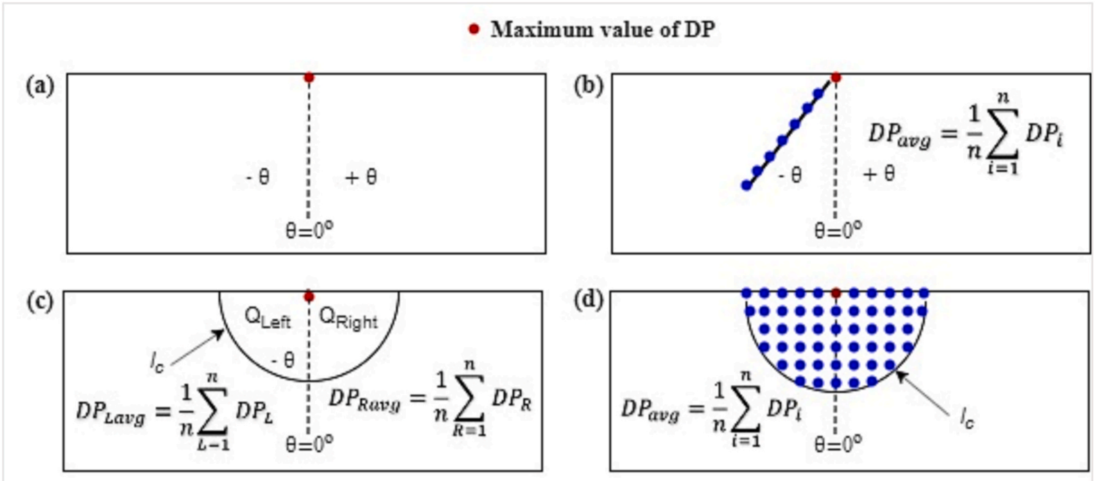

Fig. 3. Damage parameter calculation methods: (a) point (hot spot) approach, (b) line approach, (c) quadrant averaging approach, and (d) volume averaging approach.

categories: strain-based, stress-based, and strain-energy–density-based techniques. In the stress-based group, widely used models include the McDiarmid parameter (McDiarmid, 1991) and the shear stress range parameter (Lykins et al., 2001), with the Findley parameter being particularly popular. Strain-based methods include the Fatemi-Socie parameter (Fatemi and Socie, 1988) and the Brown-Miller parameter (Brown and Miller, 1973), while strain-energy–density-based approaches feature models like Smith-Watson-Topper (Smith, 1970) and Liu damage parameters (Liu, 1993). Szolwinski et al. (Szolwinski and Farris, 1996) were the first to use the critical plane approach to study fretting fatigue, and since then, several damage models originally designed for plain fatigue have been adapted for fretting fatigue analysis. In this research, the Findley Parameter (FP), Smith Watson Topper (SWT) parameter and Fatemi-Socie (FS) parameters are used.

3.2.1. Findley Parameter (FP)

FP is a stress-based damage parameter for high-cycle fatigue, which is calculated using the maximal shear stress and normal stress amplitudes. This parameter is presented in Eq. (10) as:

$$FP = \frac{\Delta\tau_{\max}}{2} + k\sigma_n^{max} \tag{10}$$

where σ_n^{max} represents the maximum normal stress, $\Delta\tau_{\max}$ denotes the maximum shear stress amplitude and k is a material constant. The value of k for Ti-6AL-4 V is taken from Kallmeyer et al. (Kallmeyer et al., 2002), who estimated it using an iterative procedure and found that $k =$ 0.30 provided the best results for FP. For IN-100 the value of k is taken as 0.35 as reported in ref. (Madhi, 2006). These k values are cited from the studies conducted on the same material used in the present study. The method for calculating crack initiation life using the Findley parameter (FP) was subsequently proposed by Park and Nelson (Park and Nelson, 2000), specifically for application in the high-cycle fatigue regime, as presented in Eq. (11).

$$FP = \tau_f'(2N_i)^{b'} \tag{11}$$

where τ_f' represents the shear fatigue strength coefficient and b' is the torsional fatigue strength exponent.

3.2.2. Smith-Watson-Topper (SWT)

SWT parameter is one of the most widely utilized parameters for calculating fretting fatigue lifetime. This parameter is mathematically expressed as the product of the peak tensile stress and the corresponding strain amplitude. Maximum principal strain amplitude was used in place of strain amplitude in Socie's (Socie, 1987) modification of the SWT parameter for enhanced accuracy:

$$SWT = \sigma_n^{max}\frac{\Delta\varepsilon_1}{2} \tag{12}$$

This criterion was used by Szolwinski (Szolwinski and Farris, 1996) for investigating fretting fatigue. They suggested that the plane most susceptible to damage, determined by the interaction between the maximum normal stress and the normal strain amplitude, is the predicted site for crack nucleation. This additional modification is shown in Eq. (13):

$$SWT = \sigma_n^{max}\frac{\Delta\varepsilon_n}{2} \tag{13}$$

where σ_n^{max} is the maximum normal stress and $\Delta\varepsilon_n$ is the normal strain amplitude.

Initiation life N_i can be related to SWT using Eq. (14):

$$SWT = \frac{\sigma_f'^2}{E}(2N_i)^{2b} + \sigma_f'\varepsilon_f'(2N_i)^{b+c} \tag{14}$$

where σ_f' denotes the fatigue strength coefficient, ε_f' denotes fatigue ductility coefficient, b denotes fatigue exponent, and c denotes the fatigue ductility exponent.

Given that the applied loads in the fretting fatigue tests did not surpass the material's yield stress, the stress conditions can be considered purely elastic. Simplifying Eq. (14) yields:

$$SWT = \frac{\sigma_f'^2}{E}(2N_i)^{2b} \tag{15}$$

3.2.3. Fatemi-Socie (FS)

Fatemi and Socie (Fatemi and Socie, 1988) introduced a strain-based parameter known as FS, which takes into account the maximum shear strain amplitude γ_{max}, the maximum normal stress σ_n^{max}, and the material's tensile yield strength σ_y. The FS parameter is calculated using the following formula:

$$FS = \frac{\gamma_{max}}{2}\left(1 + k_2\frac{\sigma_n^{max}}{\sigma_y}\right) \tag{16}$$

where k_2 is the ratio of material's yield strength σ_y to tensile fatigue strength exponent.

$$k_2 = \frac{\sigma'_f}{\sigma_y} \tag{17}$$

Eq. (18) can be used to calculate initiation lifetime using FS parameter (Li et al., 2015).

$$FS = \frac{\tau'_f}{G}(2N_i)^{b'} + \gamma'_f(2N_i)^{c'} \tag{18}$$

where G is the shear modulus, γ'_f is the shear fatigue ductility coefficient and c' is the torsional fatigue ductility exponent. In the high-cycle fatigue regime, the plastic strain amplitude becomes negligible allowing the ductility term in the life equation to be omitted (Fuchs et al., 2000). All fatigue lives considered in this study fall within the high-cycle regime; therefore, Eq. (18) can be re-written as:

$$FS = \frac{\tau'_f}{G}(2N_i)^{b'} \tag{19}$$

The coefficients for Ti-6Al-4 V alloy at 260 °C are estimated from the fretting fatigue data in Ref. (Sahan, 2002), which is the same study that provided the fretting test results and corresponding material properties. The estimated values of τ'_f, σ'_f, b' are 1121.6 MPa, 1945 MPa and −0.093, respectively. For IN-100 alloy at 600°C, the values of τ'_f, σ'_f, b' are 1440 MPa, 2415 MPa and −0.086, respectively taken from Ref. (Murthy et al., 2006) which reports properties for the same material and operating temperature.

3.3. Damage parameter (DP) calculation methods

Various approaches have been proposed and utilized by researchers to calculate DP. The volume averaging approach, quadrant approach, line approach, and hot-spot approach will be briefly discussed in this section.

3.3.1. Hot-Spot approach

The hot-spot approach (Fig. 3 (a)) is frequently employed for calculating the crack initiation position and angle (Sahan, 2002; Jin et al., 2005; Lykins et al., 2001). The damage parameter is calculated in every direction. The location with peak value is considered as hotspot, i.e. the angle that corresponds to this value indicates the direction of crack. This peak value is then used to calculate the initiation life. However, under fretting conditions, the stress gradient can be quite steep owing to loading conditions and stress concentration at critical points. It is crucial to take into account the subsurface distribution of damage parameters for improved accuracy.

3.3.2. Line approach

In this approach, DP values are averaged along predetermined radial lines as shown in Fig. 3 (b) (Araújo and Nowell, 2002). The average DP value is used to calculate the initiation life, and the angle corresponding to the peak DP value is termed the crack orientation. However, if there is a small critical zone then a limited number of averaged data points exists, which can lead to deviation in results.

3.3.3. Volume averaging approach

In this approach (Fig. 3 (d)), the point exhibiting the maximum damage parameter value is selected as semi-circular region's centre with a defined radius. The damage parameter is then averaged within this region to account for the influence of subsurface stresses. However, a notable limitation is that the predicted crack nucleation angle frequently deviates from experimental observations, suggesting that the model may not fully capture the material's behaviour or stress conditions (Infante-Garcia, 2019; Navarro et al., 2008).

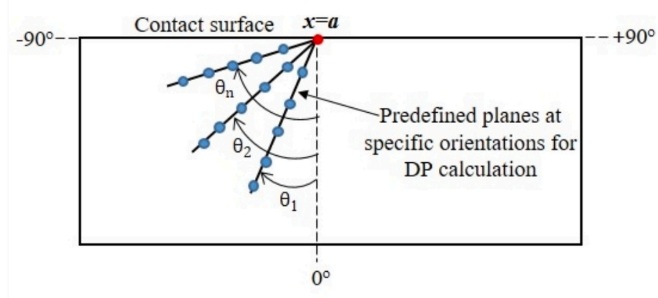

Fig. 4. Schematic of line method for crack orientation (Navarro et al., 2017).

3.3.4. Quadrant averaging approach

In the quadrant averaging approach, just like volume averaging approach a semi-circular zone is considered for stress averaging. The volume method has demonstrated good accuracy in predicting crack initiation life; however, its application to estimating the crack initiation angle can lead to errors because the stress state changes rapidly in the vicinity of the contact edge. To address this limitation, it is essential to distinguish whether a crack, immediately after initiation, propagates toward the interior of the contact zone (negative x-direction) or toward the exterior of the contact zone (positive x-direction). For this purpose, the process zone is divided into two regions: the left quadrant and the right quadrant as shown in Fig. 3 (c). This approach combines the strengths of both the line and volume methods. Specifically, it incorporates the directional sensitivity of the line method, which identifies the most critical crack plane, together with the averaging capability of the volume method, which accounts for the multiaxial stress and strain distribution within a finite material volume. The DP is computed separately in each quadrant, and the quadrant with the highest averaged DP value is considered the most probable crack initiation orientation. This methodology enables a more realistic assessment of crack initiation direction by capturing the asymmetry in stress gradients near the contact edge, which are not adequately resolved by volume averaging method alone. The initiation life is calculated based on the maximum averaged DP value (Bhatti et al., 2019). However, it was shown that crack orientation using this method depends on the averaging dimension. Also, the quadrant method will produce similar result as hotspot method when employed using SWT because of only one peak value in both quadrants.

3.3.5. Proposed method for crack orientation

Navarro et al. (Navarro et al., 2017) proposed a modified line method for prediction of early crack paths under fretting fatigue loadings. In contrast to the traditional line method, DP values are computed along fixed material planes oriented at the same angle as the line. In this method (Fig. 4), several predefined lines are drawn in a 2D plane (−90° to + 90°) from the trailing edge of the contact surface at different orientations (θ_1, $\theta 2$,…,θ_n). For each line, the DP is computed at every node along the line based on a fixed material plane orientation corresponding to the angle θ of the line. This differs from the CP method, where, at each node, the DP is calculated for all possible plane orientations, and the orientation corresponding to the maximum value is selected as critical plane. It was proposed that since all points along the defined straight line are evaluated using the same material plane orientation for the fatigue criterion parameter, it is reasonable to hypothesize that lines exhibiting higher average values are more susceptible to crack initiation.

Based on this modified line method, we propose a new averaging method termed as zone-based method. According to the proposed methodology, the crack initiation location is first identified using the conventional critical plane approach. Specifically, the point along the contact surface that maximizes the critical plane fatigue parameter is selected as the initiation site. Taking this point as the centre, the

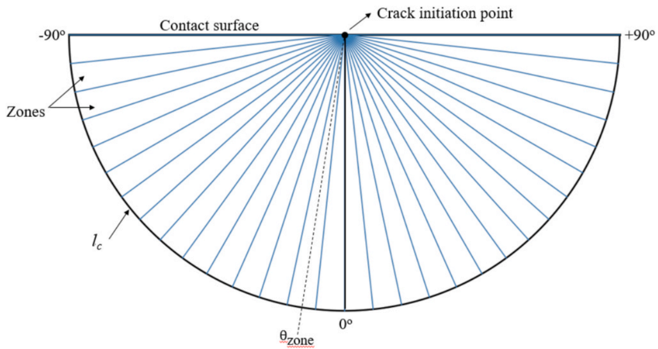

Fig. 5. Schematic of the proposed zone based method.

subsurface region beneath the contact is then discretized into multiple angular zones as shown in Fig. 5. Each zone extends radially from this centre, with a radius equal to the critical distance. The angular resolution chosen for subdividing the subsurface region beneath the contact has a direct impact on the number of finite elements available within each zone. A smaller angular increment results in fewer elements per zone. To maintain an appropriate balance between directional resolution and sufficient number of elements for computing damage parameters, the subsurface region is divided into 30 angular zones, each spanning 6° extending from − 90° to + 90°. In the line-based method, only elements along each line are considered, often resulting in a small number of points and potentially missing localized damage in neighbouring elements. In contrast, the zone-based method averages over a larger number of elements within each angular sector, which not only improves statistical reliability but can also yield higher mean DP values by capturing broader regions of high damage.

To increase the robustness of analysis the mesh size in the contact area was reduced to 1 μm. This refinement was necessary to increase the number of finite elements within each angular zone. Sub-modelling technique was implemented to manage computational cost.

In each zone, the multiaxial fatigue parameters are computed using a material plane coincident with central orientation of that zone. For example, in the zone extending from − 90° to − 84°, the evaluation of DP is performed using a plane oriented at − 87°. The mean value of each fatigue damage parameter is computed within each zone, and the zone exhibiting the highest mean value is identified as the most likely orientation for crack initiation. The fretting fatigue initiation life is subsequently estimated based on the mean DP values within this critical zone. Since all zones converge at the crack initiation point, so elements near this point are shared between multiple adjacent zones. For such shared elements, the damage parameter (DP) is recalculated separately for each zone using respective zone's central orientation (θzone). These values are then included in the averaging of their respective zones, ensuring the shared elements contribute equally to every zone. The influence of rapidly changing stress near contact surface was investigated by Araújo and Nowell (Araújo and Nowell, 2002). Their results showed an improved prediction accuracy of fatigue life using material's grain size as averaging dimension. The critical radius of 20 μm is selected for this study for Case 1 (Bhatti et al., 2018) and 100 μm for Case 2 being the grain size of the materials (Ownby, 2008).

4. Numerical model

A two-dimensional numerical model is constructed in this work to model the fretting fatigue specimen involving a cylindrical pad and a flat specimen. The contact problem is solved using a commercially available software, ABAQUS. Only half of the experimental arrangement is included in the numerical model due to its symmetry. The material properties of Ti-6Al-4 V alloy at 260 °C and IN-100 alloy at 600 °C are utilized in the analysis. These properties include a modulus of elasticity (E) of 95 GPa, coefficient of thermal expansion (CTE) of 9.4×10^{-6} °C^{-1} and a Poisson's ratio of 0.33 for Ti-6Al-4 V (Jin et al., 2005). For IN-100 the material properties are: a modulus of elasticity (E) of 193 GPa, a coefficient of thermal expansion (CTE) of 8.0×10^{-6} °C^{-1} and a Poisson's ratio of 0.3 (Mall, 2010). The numerical model consists of a cylindrical pad with a rectangular specimen. Both specimen and pad have the same thickness of 6.35 mm. The specimen is restrained at the bottom in y-direction whereas both sides of the pad are retrained in x-direction. Radius of the cylindrical pad is 50.8 mm and the dimensions of test specimen are 19.25mm × 1.905mm. Predefined field option in ABAQUS is utilized to define the temperature of the analysis in step 1. Initial value of temperature is set to room temperature (20 °C), which is then extended to 260 °C and 600 °C for Case 1 and Case 2, respectively. Room temperature numerical simulations were also performed to understand the effect of temperature on contact conditions and CP parameters as presented in Section 5. The elastic modulus is made temperature-dependent in the finite element analysis. For Case 1 the values of elastic modulus used for room temperature and high temperature analysis are 126 GPa and 95 GPa For Case 2 these values are 215 GPa and 193 GPa (Shu et al., 2024; , xxxx). A constant CoF is applied in the numerical simulations having value 0.55 and 0.4 for Case 1 and Case 2,

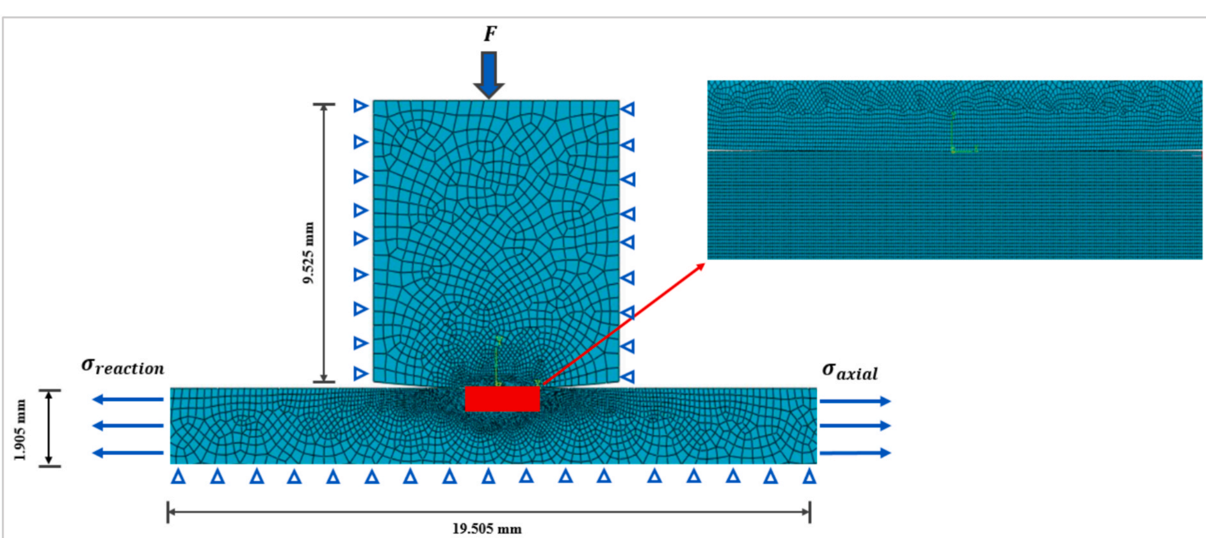

Fig. 6. Two-dimensional numerical model of the fretting fatigue problem.

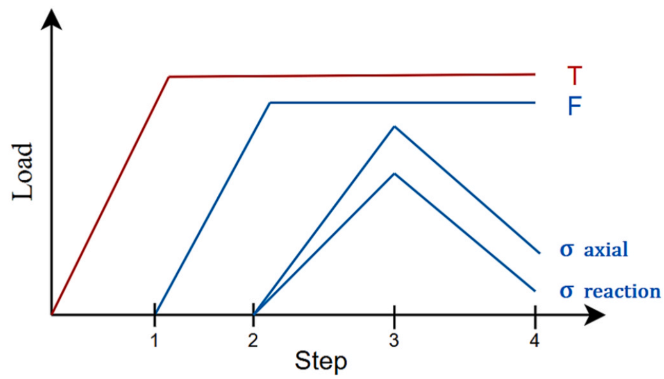

Fig. 7. Applied loading sequence for temperature, normal load, axial load and reaction load.

respectively. A normal load F with a constant amplitude is applied on the upper side of the pad (Fig. 6). Axial stress is applied to the specimen's right side, whereas reaction stress is applied to the other end of the test specimen. Eq. (20) is used to compute the reaction stress as follows:

$$\sigma_{\text{reaction}} = \sigma_{\text{axial}} - \frac{Q}{A} \tag{20}$$

where A represents the area cross section of the test specimen. The applied temperature and loading sequence are shown in Fig. 7.

Lykins et al. (Lykins et al., 2000) showed that, for elastic fretting contacts in finite element analysis, a single loading cycle is sufficient to capture the fretting fatigue response. They reported that key results, including contact pressure, shear traction, and stress distributions, remain unchanged after the first cycle, thereby justifying the use of a single cycle for evaluating CP parameters. An element size of 4 μm x 4 μm is used to improve the mesh in the contact zone and is getting coarser while moving away from the contact region. CPE4R, a 4-node bilinear quadrilateral plane strain element with decreased integration, is the element type that is employed. The top surface of the specimen is identified as the slave surface in this model, while the cylindrical surface of the pad is assigned as the master surface. These surfaces' contact conditions are defined by a main-secondary algorithm.

To improve the accuracy of contact stresses, a surface-to-surface contact approach is employed between the specimen and the pad by allowing each secondary surface node to interact with multiple main surface facets. The main and secondary surfaces contact tracking is applied through the application of a finite sliding concept. In order to accurately model fretting problem, Lagrange multiplier approach is utilized for frictional formulation since it retains zero relative slip under stick conditions and firmly enforces the pressure-penetration relationship.

CP approach is implemented by solving the model using ABAQUS and Python scripting is then utilized for post-processing. The required stress and strain data across the contact width (from $-a$ to a) is stored for further use. To determine the maximum DP, Mohr's circle transformation is applied to transform the stress and strain values, and the plane is rotated from -90° to 90° in 1° increments. For each increment, the values of FP, SWT and FS are recorded for a node. The values of DP for each node are compared for all increments and the maximum value and corresponding plane orientation are stored. DP values for all nodes are then compared. The node with peak DP value is identified as crack imitation site, and the corresponding value is used to calculate crack initiation lifetime using Eq. (11), Eq. (15) and Eq. (19). To apply the zone-based method, the mean value of DP in the critical zone is utilized. Subsequently, the crack initiation orientation is predicted to occur in the zone exhibiting the higher mean value. The mean value is then employed to get the initiation life using Eq. (11), Eq. (15) and Eq. (19). The plastic deformation characteristics of materials are typically less critical under fretting conditions, particularly in the context of high-cycle fatigue (HCF), where stress amplitudes remain relatively low, and deformation remains predominantly elastic (Wang et al., 2023). Therefore, plasticity was not considered in this investigation.

Table 3
FEA and analytical solutions contact width and peak contact stress.

	Case 1 Analytical	Numerical	Case 2 Analytical	Numerical
Half Contact Width (mm)	0.51	0.515 **(0.77)**	0.62	0.618 **(0.32)**
Peak Contact Stress (MPa)	262	260 **(0.76)**	648	660 **(1.81)**

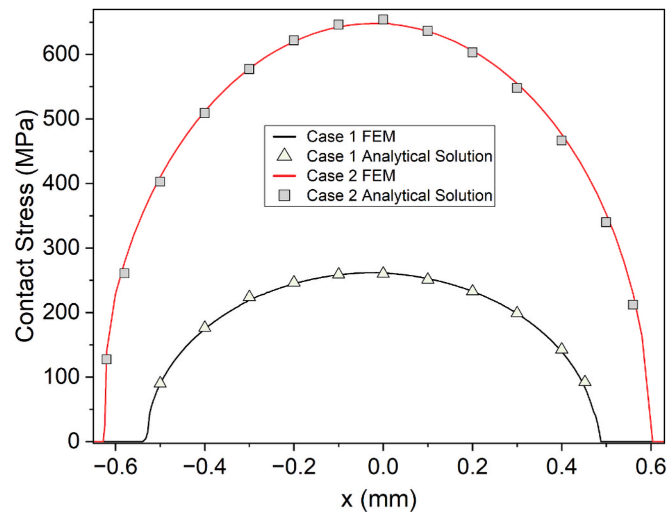

Fig. 8. Analytical and numerical contact stress distributions for both cases.

Table 4
Contact width and peak contact stress comparison at room and high temperatures.

	Case 1 Room Temperature	High Temperature	Case 2 Room Temperature	High Temperature
Half Contact Width (mm)	0.45	0.51	0.59	0.62
Peak Contact Stress (MPa)	298	260	686	660

5. Results and discussion

5.1. Model validation

To ensure that the contact and boundary conditions are proper and reflect the experimental conditions well, the numerical model is validated using analytical solutions for peak value of contact stress and contact width. Test 1 from both cases is selected for comparison between the numerical and the analytical results. Table 3 shows that the percentage error between analytical and numerical solutions for given parameters is less than 2 % for each case. Fig. 8 presents the contact stress profiles for both material cases, with analytical solutions shown as discrete markers and finite-element results as continuous lines. In each case, the finite element solution curves closely trace the analytical data, demonstrating excellent agreement across the entire contact region. This

Table 5
Comparison of stick and slip zones at room and high temperatures.

	Room Temperature			High Temperature		
	Stick Zone (mm)	Slip Zone (mm)	Slip Amplitude (mm)	Stick Zone (mm)	Slip Zone (mm)	Slip Amplitude (mm)
Case 1	−0.40 to 0.13	−0.46 to −0.40 and 0.13 to 0.44	0.0022	−0.42 to 0.06	−0.53 to −0.424 and 0.06 to 0.50	0.0040
Case 2	−0.56 to 0.08	−0.60 to −0.56 and 0.08 to 0.58	0.0023	−0.58 to 0.05	−0.61 to −0.58 and 0.05 to 0.63	0.0031

close agreement validates our numerical model's ability to capture the Hertzian stress distribution for differing materials and supports the fidelity of subsequent fatigue analyses.

5.2. Effect of temperature on contact conditions

Table 4 provides a comparison of half contact width and peak contact stress at room and elevated temperatures. For both cases, the half contact width increases with temperature. In Case 1, it expands from 0.45 mm at room temperature to 0.51 mm at 260 °C. Case 2 shows a smaller but consistent increase from 0.59 mm to 0.62 mm at 600 °C primarily due to reduced material stiffness at elevated temperatures. A decrease in peak contact stress is observed at elevated temperatures. In Case 1, the contact stress drops from 298 MPa to 260 MPa, and in Case 2, from 686 MPa to 660 MPa due to more distributed load along a wider contact area and reduced stress concentration.

Table 5 presents a comparative analysis of the stick and slip zones and slip amplitude at room and elevated temperatures for both material systems. The results reveal a clear temperature dependency in the fretting contact response, characterized by a reduction in the stick zone length and a corresponding expansion of the slip zone under elevated temperature conditions.

In Case 1, the stick zone at room temperature spans from –0.40 mm to 0.13 mm, whereas at 260 °C, it contracts to a range of –0.42 mm to 0.06 mm. Notably, the onset of sticking contact occurs at a slightly more negative position along the *x*-axis at elevated temperature, suggesting that thermal expansion and increased compliance promote earlier engagement in the contact interface. However, the termination point of the stick zone also shifts inward, resulting in a net reduction of the stick region. Concurrently, the slip zone expands in both directions, and the slip amplitude increases from 0.0022 mm to 0.0040 mm.

A similar trend is observed in Case 2. The stick zone decreases from –0.56 mm to 0.08 mm at room temperature to –0.58 mm to 0.05 mm at 600 °C. This again indicates that at higher temperatures, the stick zone

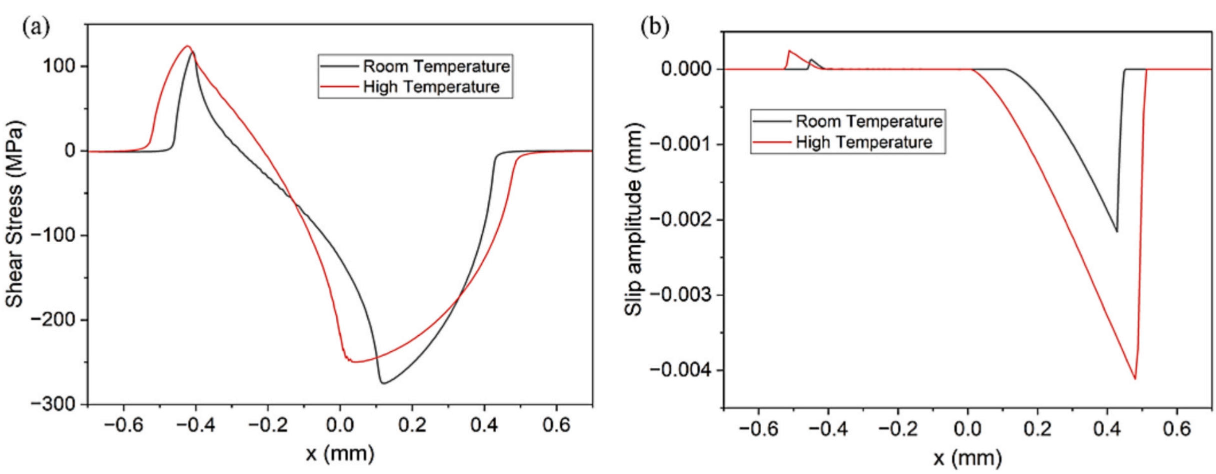

Fig. 9. Distribution of (a) shear stress and (b) slip amplitude for Case 1.

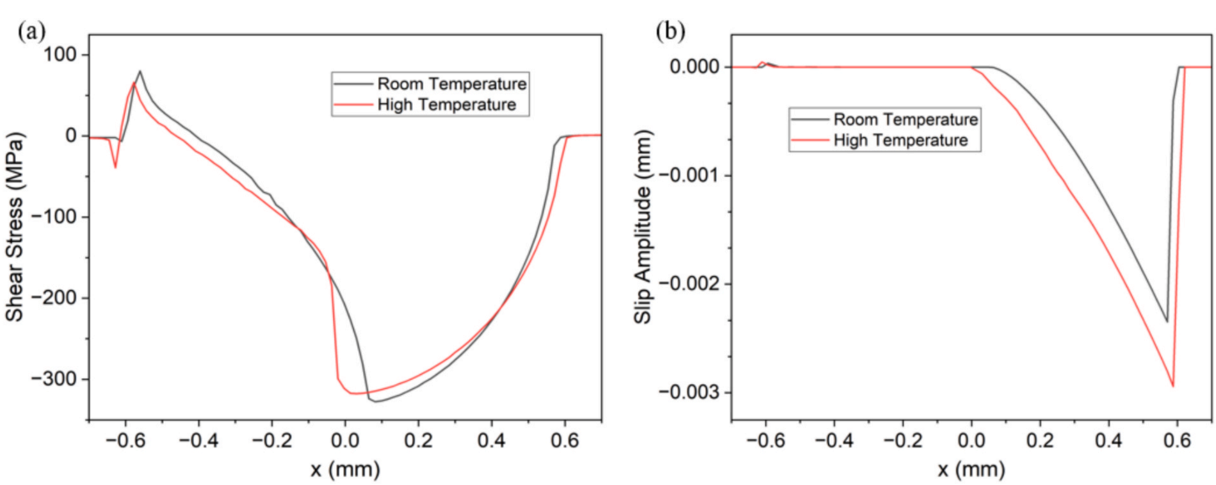

Fig. 10. Distribution of (a) shear stress and (b) slip amplitude for Case 2.

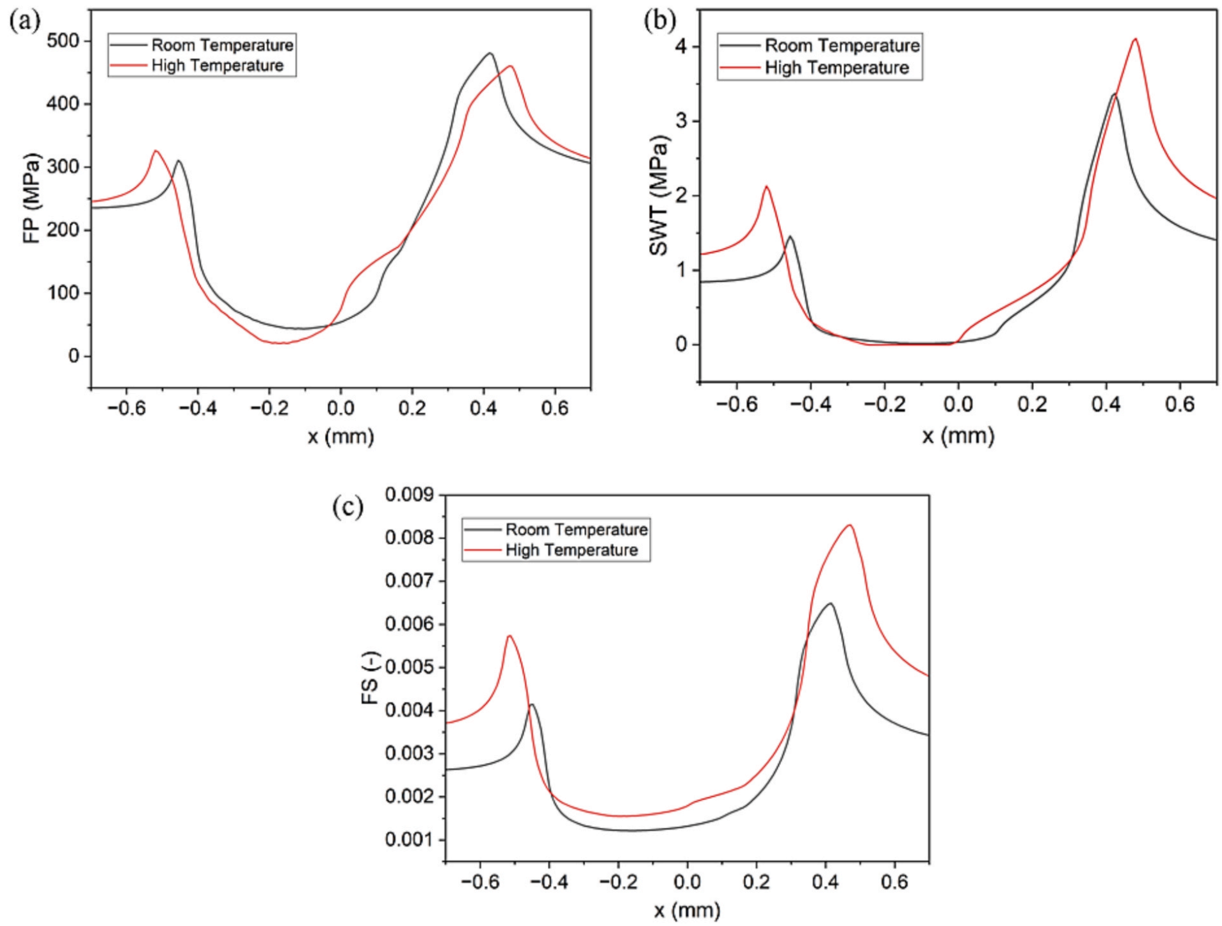

Fig. 11. Distribution of (a) FP, (b) SWT and (c) FS along the contact surface for Case 1.

starts slightly earlier and terminates sooner. The slip amplitude increases from 0.0023 mm to 0.0031 mm. These findings are corroborated by Fig. 9(a) and Fig. 10(a), which shows the shear stress profile for Case 1 and Case 2 respectively. The slip amplitude profile demonstrates a broader and deeper response at high temperature as compared to the room temperature case as shown in Fig. 9(b) and Fig. 10(b).

The increased slip amplitude near the trailing edges of the contact zone, has direct implications for fretting fatigue, as it may promote earlier crack initiation. These observations collectively suggest that elevated temperature significantly alters the stick–slip behaviour in fretting fatigue contact.

5.3. Effect of temperature on DP values

The distribution of DP values for Case 1 and Case 2 is shown in Fig. 11 and Fig. 12 respectively. In all cases, the peak values occur near the trailing edge of the contact region. At elevated temperature, the position of the peaks shift slightly toward the right, consistent with the increase in contact width. As shown in the Fig. 11(a) and 12(a), FP decreases slightly with temperature for both cases. The FP is stress-driven, relying on maximum shear stress and normal stress on the critical plane. This reduction is reflected by a slight drop in stress magnitudes as shown in Fig. 14 (a-b) due to reduced stiffness, and the free-end boundary condition that prevents build-up of axial stress in response to higher strain. A distortion is observed in the centre of Fig. 12 (a) which is unlikely to be a direct effect of temperature. Instead, it can results from the contact surface effects like high stress gradients, particularly in the stick–slip transition zone and at the contact edges. This distortion is confined to the contact surface and disappears in the FP profile plotted 40 μm below the contact surface as shown in Fig. 13. Furthermore, stress-averaging techniques have been employed to account for the high stress gradients near the contact surface. Therefore, this localized surface effect does not impact the results.

In contrast, the SWT and FS parameters both increase with temperature as shown in Fig. 11 (b-c) and Fig. 12 (b-c). These parameters are sensitive to strain amplitude, and their increase is directly related to the higher strains seen in the high-temperature condition. As shown in the strain plots in Fig. 14 (b-c), both shear and tangential strains are noticeably larger at high temperature. Even though the stress is reduced, and the specimen is free to expand at the edge, the lower stiffness and thermal strain causes greater deformation under the same loading. This leads to higher strains, which increase SWT and FS parameters. These results suggest that the damage potential is higher at elevated temperature, in agreement with the observations of increased slip amplitude and slip zone size.

The different trends seen in FP compared to SWT and FS highlight the importance of considering strain effects in high-temperature fretting fatigue. While FP tends to underestimate the damage because it relies on stress levels that decrease with temperature, SWT and FS provide a better representation of the actual damage behaviour, as they incorporate the increased deformation capacity of the material. It is also observed that the differences in fatigue parameters between room and elevated temperature are less pronounced in Case 2 compared to Case 1. This can be attributed to the lower coefficient of thermal expansion of IN-100, which limits the development of thermal strain even at 600 °C. Additionally, the reduction in elastic modulus for IN-100 is comparatively smaller, resulting in less pronounced changes in strain responses.

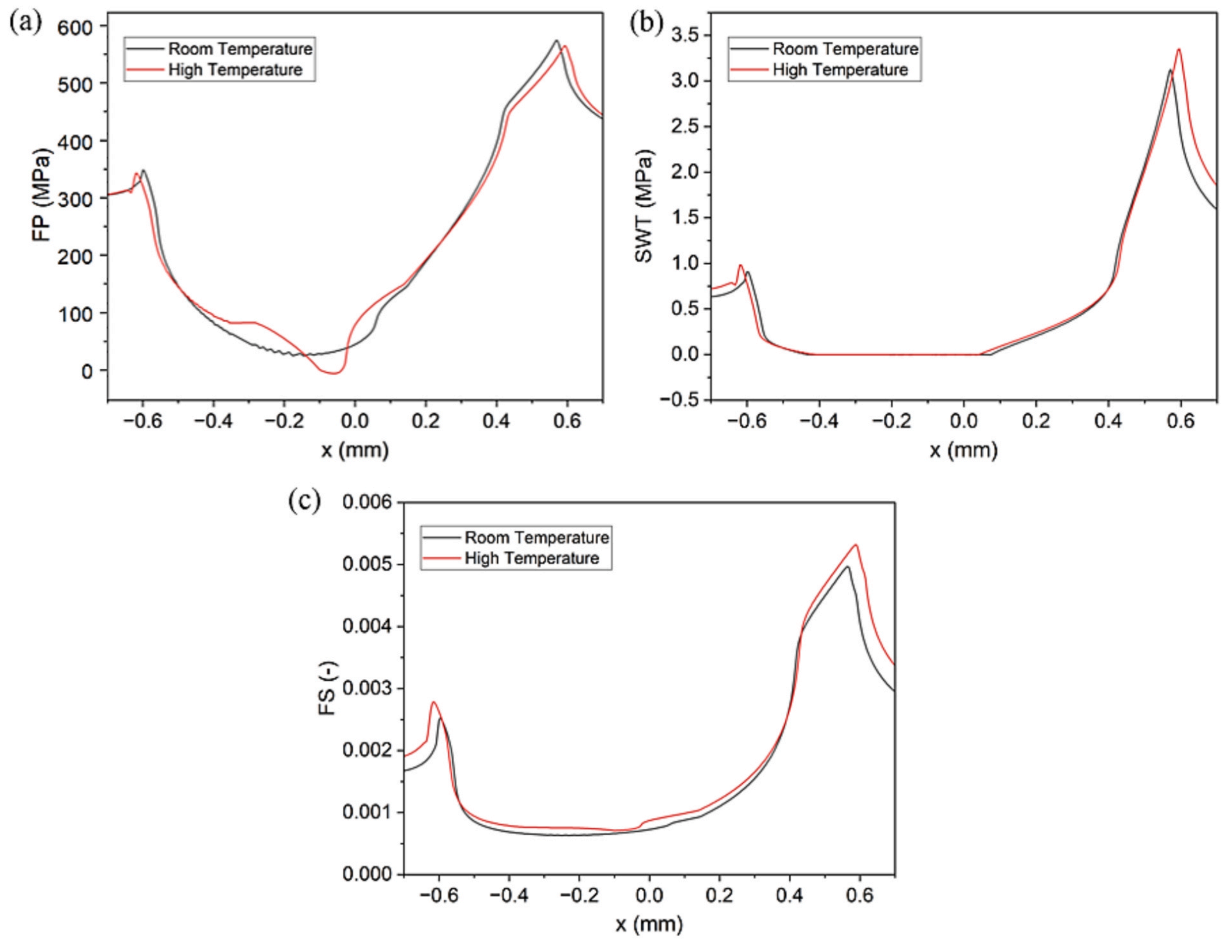

Fig. 12. Distribution of (a) FP, (b) SWT and (c) FS along the contact surface for Case 2.

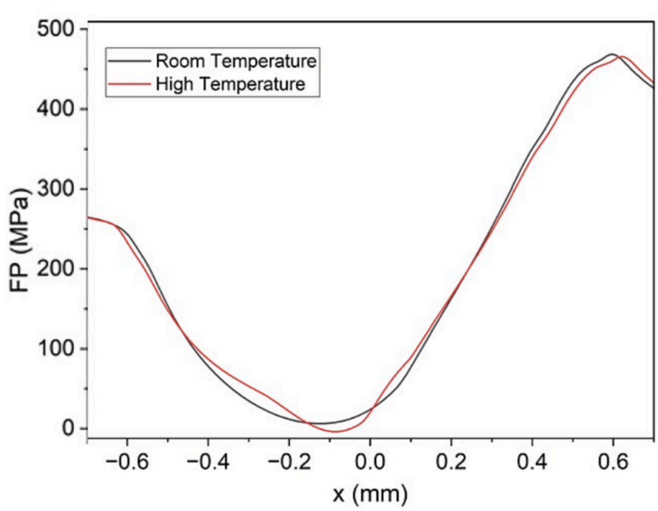

Fig. 13. Distribution of FP at a distance of 40 um beneath the contact surface for Case 2.

5.4. Crack initiation location

FP, SWT and FS near the contact area are analysed for the crack initiation position at elevate temperatures for both cases and results are compared with the experimental observations. The point corresponding to the maximum value is assumed to be the crack initiation position. The results for all the tests are shown in Table 6. Crack initiation location is presented as x/a, where a represents the contact half width. In all cases, the crack initiation site is close to the trailing edge ($x/a = 1$) of contact surface and closely align with the experimental values ($x/a \approx 1$) (Ownby, 2008; Sahan, 2002). The distribution of damage parameters near the trailing edge for test 1 is presented in Fig. 11 and Fig. 12 for Case 1 and Case 2, respectively.

5.5. Crack orientation

Table 7 presents the predicted crack initiation orientations using the hot spot method, quadrant method and zone based method for Case 1. Since the crack orientation predictions using volume method and line method are similar to hotspot method, they are not considered in this comparison (Araújo and Nowell, 2002). Experimental validation is available only for Case 1, where the observed crack angle is approximately -45° (Sahan, 2002). Given the availability of experimental data, subsequent discussion in this section will focus exclusively on Case 1 to ensure meaningful interpretation and model assessment. The predicted orientation using hotspot method by FP and FS is out of the contact region ($+\theta$), which is not in agreement with the experimental value of -45°. However, for SWT, the predicted orientation is in $-\theta$ direction but still the values are not in agreement with the experimental observations. Fig. 15(a) shows the variation of DP with angle for the FP, SWT, and FS criteria using hotspot method. The FP and FS parameters exhibit two symmetric peaks, with the maximum occurring at $+26^\circ$ and $+39^\circ$, respectively, while the corresponding negative peaks are slightly lower at -29° for FP and -43° for FS. Following the CP approach, the angle corresponding to the maximum DP is selected as the predicted crack

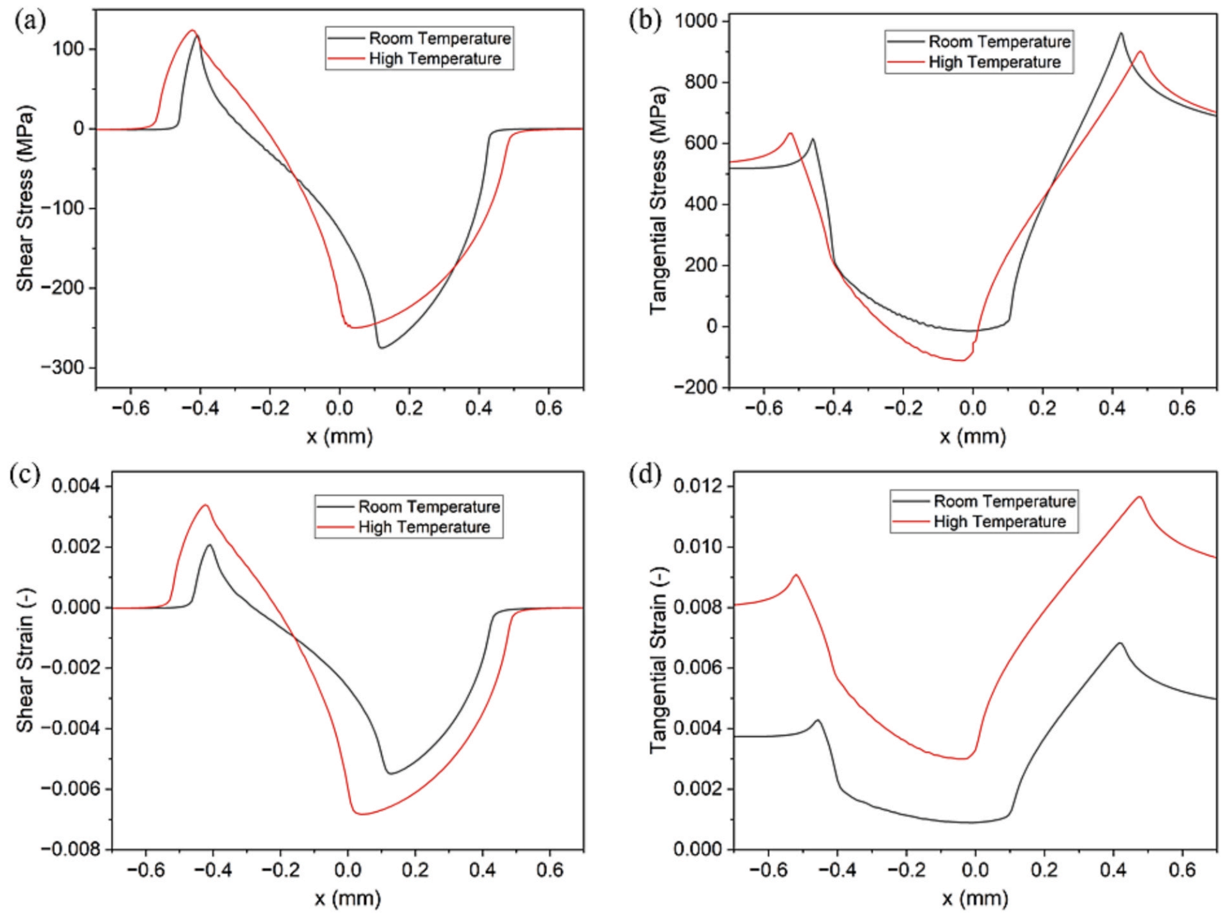

Fig. 14. Distribution of (a) shear stress, (b) tangential stress, (c) shear strain, and (d) tangential strain along the contact surface for Case 1 (test 1).

Table 6
Fretting fatigue crack location using CP parameters.

	Test Number	Crack Initiation Location x/a FP	SWT	FS
Case 1	1	0.942	0.942	0.933
	2	0.949	0.949	0.941
	3	0.949	0.949	0.941
	4	0.949	0.949	0.941
	5	0.949	0.949	0.941
	6	0.949	0.949	0.941
Case 2	1	0.957	0.964	0.951
	2	0.971	0.971	0.964
	3	0.964	0.964	0.958
	4	0.964	0.964	0.951
	5	0.964	0.964	0.958
	6	0.964	0.964	0.958
	7	0.970	0.970	0.964

initiation orientation, which falls on the positive side for both FP and FS. In contrast, SWT shows a single dominant peak at -1°.

Using the quadrant method, the results for both FP and FS shifted to negative ($-\theta$) direction. This shift is due to high average value DP in the left quadrant, suggesting a higher likelihood of crack initiation within the contact region. Although the peak value of DP is lower in left quadrant as shown in Fig. 15(a) but the average value of DP is higher in this quadrant region. The FS predictions exhibit strong agreement with experimental observations. In contrast, the FP predictions show a deviation exceeding 15° from the experimental value. The SWT criterion produced results identical to those obtained using the hotspot method, indicating that the quadrant methodology does not influence SWT predictions. The predicted orientations using the modified line method are out of the contact ($+\theta$) for FP, and into the contact ($-\theta$) for FS. The SWT predictions using the modified line method are between -5° to 5°. For the zone-based method, all predicted angle directions are into the contact region ($-\theta$), which agrees with the experimental observations. The distribution of damage parameters is presented in Fig. 15(b), where the dominants peak for FP and FS are in the negative angle range, while

Table 7
Crack orientation values using hotspot method, quadrant method, modified line method and zone-based method.

Test Number	HotspotMethod θ_{FP}(°)	θ_{SWT}(°)	θ_{FS}(°)	QuadrantMethod θ_{FP}(°)	θ_{SWT}(°)	θ_{FS}(°)	Modified line method θ_{FP}(°)	θ_{SWT}(°)	θ_{FS}(°)	Zone-basedmethod θ_{FP}(°)	θ_{SWT}(°)	θ_{FS}(°)	Experimental orientation (°)
1	26	−1	39	−29	−1	−43	55	−5	−70	−57	−15	−51	−45 (Sahan, 2002)
2	26	−1	39	−27	−1	−42	50	0	−75	−63	−9	−51	
3	25	−2	38	−26	−2	−42	55	0	−65	−57	−9	−57	
4	25	−1	38	−26	−1	−43	55	−5	−70	−51	−15	−57	
5	26	−2	36	−27	−2	−42	50	5	−65	−63	−9	−51	
6	25	−2	36	−26	−2	−43	55	5	−70	−57	−15	−57	

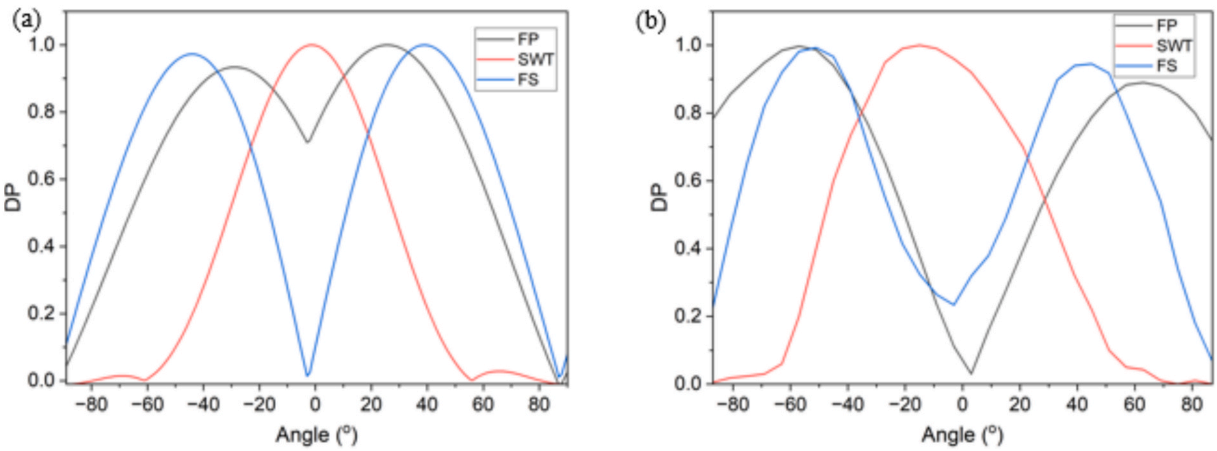

Fig. 15. Variation of critical plane parameters with angle for Case 1: (a) hotspot method, and (b) zone-based method.

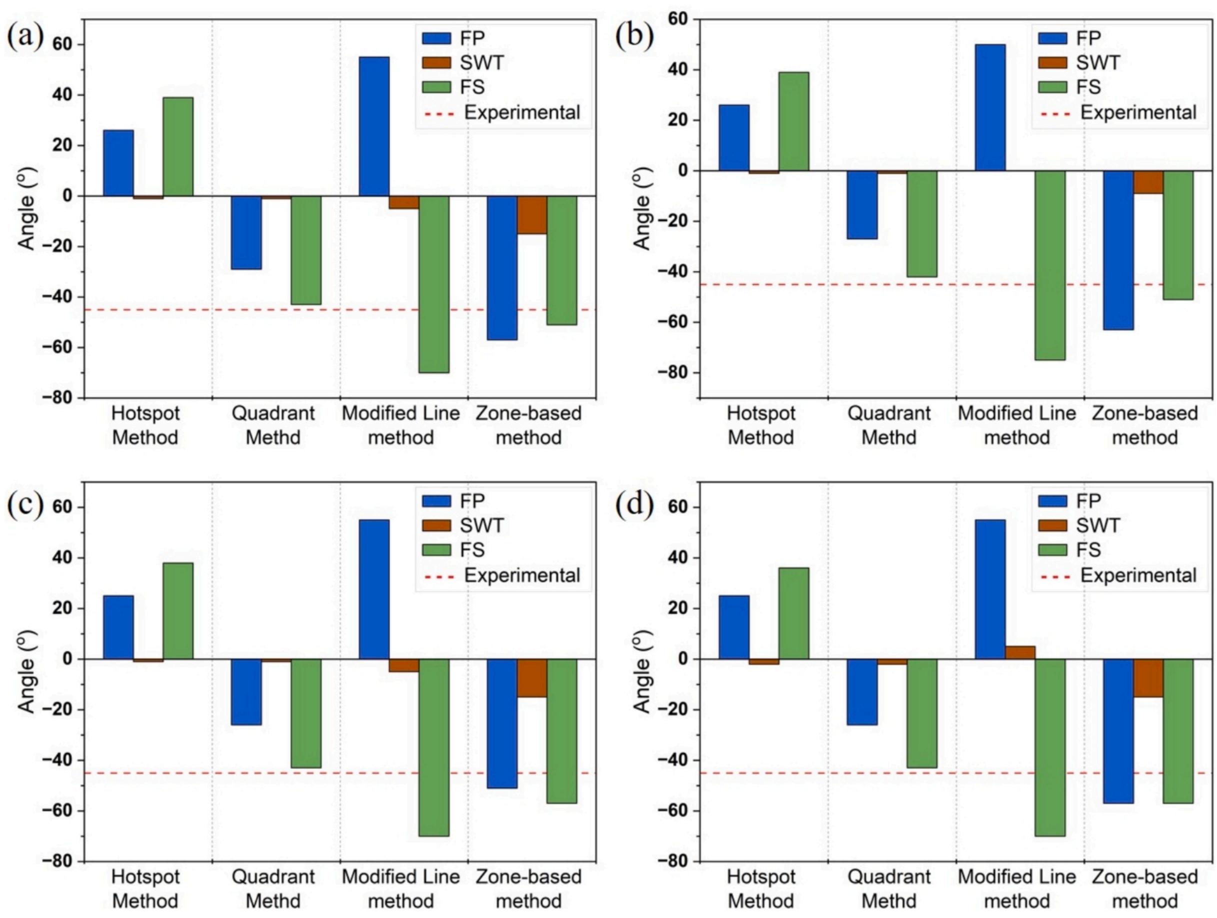

Fig. 16. Comparison of crack orientation predictions for (a) test 1, (b) test 2, (c) test 4, and (d) test 6.

SWT exhibits only one broader peak. Both FP and FS provide improved estimations, with values ranging from –51° to –63°. However, FS demonstrates slightly better accuracy and consistency, with predicted angles ranging from –51° to –57°. Although SWT shows less precision, predicting orientations between –9° and –15°, it still reflects an improvement as compared to hotspot method, modified line method and quadrant method. The comparison of different methods used for predicting crack orientation in this study for test 1, test 2, test 5, and test 6 is presented in Fig. 16.

In comparison to the quadrant method as shown in Fig. 16, the zone-based approach yields improved predictions using FP. Except for Test 2 and Test 5, all predicted FP orientations fall within a 15° deviation from experimental value, indicating enhanced accuracy than quadrant method in most cases. However, for FS, the quadrant method provides better agreement with experimental observations than the zone-based method.

5.6. Crack initiation lifetime

A comparison between experimental and predicted number of cycles

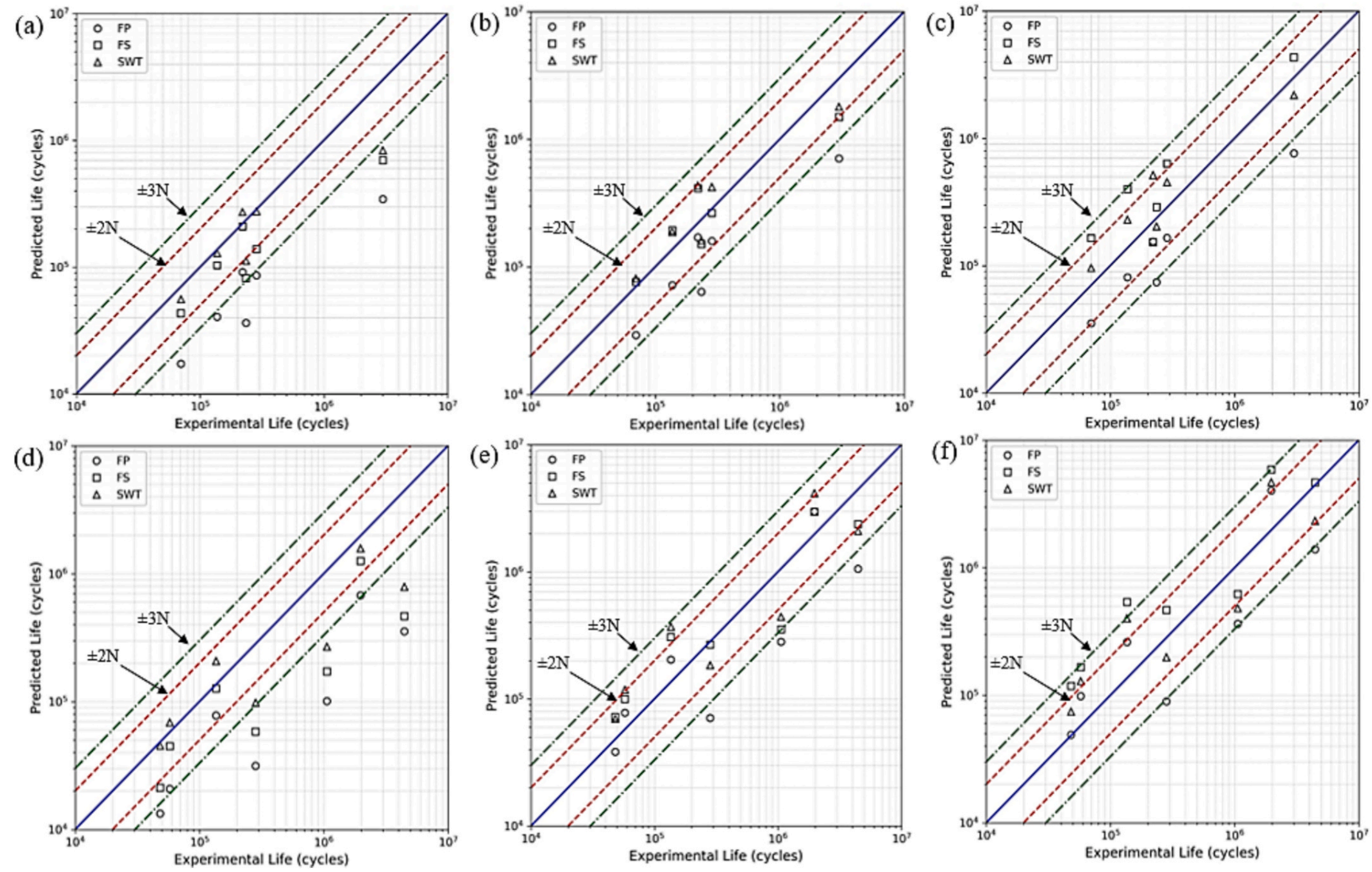

Fig. 17. Crack initiation lifetime for (a) Case 1 using hotspot method, (b) Case 1 using quadrant method, (c) Case 1 using zone-based method, (d) Case 2 using hotspot method, (e) Case 2 using quadrant method, and (f) Case 2 using zone-based method.

to initiation using hotspot method, quadrant method and zone-based method is shown in Fig. 17. Although the zone-based method is intended for crack orientation predictions, however, it is included in this section for comparison purposes. Since the experimental data reports total lifetime as presented in Table 1 and Table 2, and the previous studies in literature (Mall, 2010; Sahan, 2002; Jin et al., 2005) indicated that crack initiation constituted approximately 90 % of the total lifetime. Therefore, we assumed 90 % of the total lifetime from Table 1, to represent the initiation phase for comparison purposes.

Fig. 17(a) presents the comparison between experimental and predicted crack initiation lives using the hotspot method for Case 1. Among the three parameters, FS and SWT show better predictive performance compared to FP. Most of the data points for FP lie outside the ± 3 N scatter band, indicating poor agreement with experimental values. In contrast, FS and SWT predictions are more consistent, with all data points, except for Test 6, falling within the ± 3 N band. However, even for FS and SWT, the predictions tend to be conservative. This is primarily due to the hotspot method relying on the maximum value of the damage parameter on the contact surface, which is elevated due to stress concentration near the trailing edge of the contact. The results for Case 1 using the quadrant method are presented in Fig. 17(b). A significant improvement is observed for both FS and SWT, as all data points lie within the ± 2 N band. FP still shows some discrepancies, with Test 2 and Test 6 lying outside the ± 3 N band Fig. 17(c) presents the results for Case 1 using the zone-based method. All predictions using FS and SWT fall within the ± 3 N scatter band, indicating better agreement with experimental data as compared to hotspot method. Predictions using the zone-based method tend to be less conservative than those obtained with the quadrant method. This is primarily because DP values are computed along predefined planes rather than along the planes that maximize the DP. Consequently, compared to the quadrant method, fewer data points fall within the ± 2 N band. Between FS and SWT, the latter performs slightly better, with five data points falling within the ± 2 N band. Furthermore, SWT appears less sensitive to the averaging process compared to FS and FP, which is consistent with observations reported in Ref. (Bhatti et al., 2019).

Fig. 17(d) shows the results for Case 2 using the hotspot method. The predictions are generally conservative, with a significant deviation from experimental lives, particularly at lower stress levels. The formation of oxide layer was reported in the experimental study (Ownby, 2008) from which the fretting test data for IN-100 at 600 °C were obtained. In that study, the authors noted that oxide layer formation under high temperature conditions was more pronounced at lower stress levels. The deviation between the numerical and experimental lives at lower stress levels can likely be attributed, at least in part, to this effect, as the current numerical model does not account for the influence of oxidation at elevated temperatures. Fig. 17(e) presents the results for Case 2 using the quadrant method. As observed in Case 1, prediction accuracy improves, with all FS and SWT data points falling within the ± 3 N scatter band. However, the deviation from the line of perfect agreement is greater compared to Case 1. The FP results are less satisfactory, with three data points falling outside the ± 3 N scatter band. The zone-based method results for Case 2 are presented in Fig. 17(f). Both FS and SWT estimations demonstrate significant improvement compared to hotspot method. All SWT predictions fall within the ± 3 N scatter band, indicating good agreement with experimental results. FS predictions also show reasonable accuracy, with the exception of Test 2, which lies outside the ± 3 N band. However, in comparison to Case 1, the overall deviation from the perfect agreement line is more pronounced for all methods. Overall, the strain-based FS and the strain energy-based SWT parameters consistently provide more accurate life predictions than the stress-based FP parameter across both materials and methods. This suggests that multiaxial fatigue parameters incorporating strain effects are better suited for modelling fretting fatigue crack initiation under the elevated temperature conditions.

6. Conclusion

This study presents a comprehensive numerical investigation into the fretting fatigue crack initiation behaviour of Ti-6Al-4 V and IN-100 alloys in elevated temperatures. The predictive capabilities of three multiaxial fatigue parameters, FP, FS, and SWT, are evaluated. The following summarizes the main conclusions of this investigation:

(1) Elevated temperatures substantially influence the fretting fatigue contact conditions by promoting an increase in slip zone length and reduction in the stick zone length, due to enhanced material compliance and thermal strain effects.
(2) The stress-based FP is not suitable for high-temperature fretting fatigue applications particularly for predicting crack initiation life, as it does not account for the elevated strain levels induced by thermal expansion and reduced material stiffness.
(3) The predicted crack initiation sites show a good agreement with experimental data, being located near the trailing edge of the contact area. The zone-based method shows better accuracy in predicting crack orientation as compared to other methods.
(4) The initiation life is changed significantly when considering subsurface damage parameter values. FP and SWT lifetime predictions accuracy using the zone-based is better than hotspot method but slightly lower than quadrant method.

For future work, the focus will be to analyse crack propagation behaviour at high temperatures. In the current study, a percentage of the total lifetime for crack propagation was assumed based on literature, as discussed earlier. Therefore, the next logical step is to perform a detailed crack propagation analysis to validate this assumption and accurately compute the propagation lifetime. Furthermore, since the elevated temperature increase the slip amplitude, future work will explore the extent to which fretting wear influences crack initiation and propagation predictions at high temperatures.

CRediT authorship contribution statement

Bilal Ahmed: Writing – original draft, Validation, Methodology, Investigation. **Can Wang:** Software, Methodology. **Dagang Wang:** Writing – review & editing. **Yunlai Zhou:** Writing – review & editing. **Lihua Wang:** Writing – review & editing, Supervision. **Magd Abdel Wahab:** Writing – review & editing, Supervision, Investigation, Conceptualization.

Declaration of competing interest

The authors declare that they have no known competing financial interests or personal relationships that could have appeared to influence the work reported in this paper.

Acknowledgement

Higher Education Commission (HEC) of Pakistan provided a PhD fellowship, which the first author acknowledges. This work is supported by the National Natural Science Foundation of China (Project no. 12272270) and the Shanghai Pilot Program for Basic Research. This study is financially supported by the Natural Science Basis Research Plan in Shaanxi Province of China (2023-JC-YB-007). This work is supported by the National Natural Science Foundation of China (Project no. 52175205 and Project no. 51875565).

Data availability

Data will be made available on request.

References

Waterhouse, R.B., Fretting fatigue. 1981: Elsevier Science & Technology.
Li, C., Sun, Y., Bell, T., 1999. Consideration of fretting fatigue properties of plasma nitrided. Surf. Eng. 15 (2), 149.
Golden, P.J., Naboulsi, S., 2012. Hybrid contact stress analysis of a turbine engine blade to disk attachment. Int. J. Fatigue 42, 296–303.
Yang, Q., et al., 2019. Investigation of shot peening combined with plasma-sprayed CuNiIn coating on the fretting fatigue behavior of Ti-6Al-4V dovetail joint specimens. Surf. Coat. Technol. 358, 833–842.
Mangardich, D., Abrari, F., Fawaz, Z., 2019. A fracture mechanics based approach for the fretting fatigue of aircraft engine fan dovetail attachments. Int. J. Fatigue 129, 105213.
Su, Y., et al., 2019. Effects of secondary orientation and temperature on the fretting fatigue behaviors of Ni-based single crystal superalloys. Tribol. Int. 130, 9–18.
Chen, H., et al., 2019. Introduction of fretting-contact-induced crack closure: Numerical simulation of crack initiation and growth path in disk/blade attachment. Chin. J. Aeronaut. 32 (8), 1923–1932.
Nikitin, A.D., Shesterkin, P.S., Lopatin, S.S., 2023. Fracture of aircraft titanium alloys under high-frequency loading. SN Appl. Sci. 5 (2), 68.
Shi, D., et al., 2017. Failure assessment of the first stage high-pressure turbine blades in an aero-engine turbine. Fatigue & Fracture of Engineering Materials & Structures 40 (12), 2092–2106.
Sujata, M., et al., 2013. Fretting fatigue in aircraft components made of Ti-Al-V alloys. Procedia Eng. 55, 481–486.
Kuang, W., et al., 2022. Fretting wear behaviour of machined layer of nickel-based superalloy produced by creep-feed profile grinding. Chin. J. Aeronaut. 35 (10), 401–411.
Almeida, G.M.J., et al., 2023. Fretting fatigue of Inconel 718 at room and elevated temperatures considering both constant and cyclic normal contact loads. Tribol. Int. 183, 108382.
Wang, J., et al., 2024. Finite element analysis of fretting fatigue properties of GH4169 superalloy considering the surface treatments. Int. J. Fatigue 183, 108266.
Mall, S., et al., 2010. High temperature fretting fatigue behavior of IN100. Int. J. Fatigue 32 (8), 1289–1298.
Ownby, J.F., The effect of elevated temperature on the fretting fatigue behavior of nickel alloy IN-100., MSc thesis, 2008, Air University, USA.
Sun, S., et al., 2024. An arc-tenon attachment for nickel-based single crystal turbine blade with improved high-temperature fretting fatigue performance. Int. J. Fatigue 178, 108004.
Qu, Z., et al., 2021. Fretting Fatigue Experiment and Finite Element Analysis for Dovetail Specimen at High Temperature. Appl. Sci. 11 (21), 9913.
Zhai, Y., et al., 2020. Very high cycle fretting fatigue damage and crack path investigation of Nimonic 80A at elevated temperature. Int. J. Fatigue 132, 105345.
Sunde, S.L., Haugen, B., Berto, F., 2021. Experimental and numerical fretting fatigue using a new test fixture. Int. J. Fatigue 143, 106011.
Yuan, T., et al., 2023. Improving high temperature fretting fatigue performance of nickel-based single crystal superalloy by shot peening. Int. J. Fatigue 171, 107563.
Sahan, O., Fretting fatigue behavior of a titanium alloy Ti-6Al-4V at elevated temperature. 2002.
Jin, O., Mall, S., Sahan, O., 2005. Fretting fatigue behavior of Ti–6Al–4V at elevated temperature. Int. J. Fatigue 27 (4), 395–401.
Albinali, S., Effects of Temperature and Shot-Peening Intensity on Fretting Fatigue Behavior of Titanium Alloy TI-6AL-4V. 2005: p. 154.
Hu, C., et al., 2019. Experimental and numerical study of fretting fatigue in dovetail assembly using a total life prediction model. Eng. Fract. Mech. 205, 301–318.
Bhatti, N.A., Wahab, M.A., 2018. Fretting fatigue crack nucleation: a review. Tribol. Int. 121, 121–138.
Bhatti, N.A., Wahab, M.A., 2017. A numerical investigation on critical plane orientation and initiation lifetimes in fretting fatigue under out of phase loading conditions. Tribol. Int. 115, 307–318.
Lykins, C.D., Mall, S., Jain, V.K., 2001. Combined experimental–numerical investigation of fretting fatigue crack initiation. Int. J. Fatigue 23 (8), 703–711.
Lykins, C.D., Mall, S., Jain, V., 2000. An evaluation of parameters for predicting fretting fatigue crack initiation. Int. J. Fatigue 22 (8), 703–716.
Naboulsi, S., Mall, S., 2003. Fretting fatigue crack initiation behavior using process volume approach and finite element analysis. Tribol. Int. 36 (2), 121–131.
Li, X., Zuo, Z., Qin, W., 2015. A fretting related damage parameter for fretting fatigue life prediction. Int. J. Fatigue 73, 110–118.
Pereira, K., Bhatti, N., Wahab, M.A., 2018. Prediction of fretting fatigue crack initiation location and direction using cohesive zone model. Tribol. Int. 127, 245–254.
Szolwinski, M.P., Farris, T.N., 1998. Observation, analysis and prediction of fretting fatigue in 2024-T351 aluminum alloy. Wear 221 (1), 24–36.
Goh, C.-H., et al., 2001. Polycrystal plasticity simulations of fretting fatigue. Int. J. Fatigue 23, 423–435.
Proudhon, H., Fouvry, S., Buffière, J.-Y., 2005. A fretting crack initiation prediction taking into account the surface roughness and the crack nucleation process volume. Int. J. Fatigue 27 (5), 569–579.
Hojjati-Talemi, R., et al., 2014. Prediction of fretting fatigue crack initiation and propagation lifetime for cylindrical contact configuration. Tribol. Int. 76, 73–91.

Walvekar, A.A., et al., 2014. An experimental study and fatigue damage model for fretting fatigue. Tribol. Int. 79, 183–196.
Bhatti, N.A., Pereira, K., Abdel Wahab, M., 2019. Effect of stress gradient and quadrant averaging on fretting fatigue crack initiation angle and life. Tribol. Int. 131, 212–221.
Williams, J.A., Dwyer-Joyce, R.S., 2001. Contact between solid surfaces. Modern Tribology Handbook 1, 121–162.
Mindlin, R.D., Compliance of elastic bodies in contact. 1949.
Mindlin, R.D. and H. Deresiewicz, Elastic spheres in contact under varying oblique forces. 1953.
Nowell, D., Dini, D., Hills, D., 2006. Recent developments in the understanding of fretting fatigue. Eng. Fract. Mech. 73 (2), 207–222.
Findley, W.N., J. Coleman, and B. Hanley, Theory for combined bending and torsion fatigue with data for SAE 4340 steel. Technical Report No. 1 on basic research on fatigue failures under combined stress. 1956, Brown Univ., Providence. Engineering Materials Research Lab.
Findley, W.N., 1959. A theory for the effect of mean stress on fatigue of metals under combined torsion and axial load or bending. Journal of Engineering for Industry 81 (4), 301–305.
McDiarmid, D., 1991. A general criterion for high cycle multiaxial fatigue failure. Fatigue & Fracture of Engineering Materials & Structures 14 (4), 429–453.
Lykins, C., Mall, S., Jain, V., 2001. A shear stress-based parameter for fretting fatigue crack initiation. Fatigue & Fracture of Engineering Materials & Structures 24 (7), 461–473.
Fatemi, A., Socie, D.F., 1988. A critical plane approach to multiaxial fatigue damage including out-of-phase loading. Fatigue & Fracture of Engineering Materials & Structures 11 (3), 149–165.
Brown, M.W., Miller, K.J., 1973. A Theory for Fatigue failure under Multiaxial Stress-Strain Conditions. Proceedings of the Institution of Mechanical Engineers 187 (1), 745–755.
Smith, K., 1970. A stress-strain function for the fatigue of metals. J. Mater. 5, 767–778.
Liu, K., 1993. A method based on virtual strain-energy parameters for multiaxial fatigue life prediction, in advances in multiaxial fatigue. ASTM International.
Szolwinski, M.P., Farris, T.N., 1996. Mechanics of fretting fatigue crack formation. Wear 198 (1–2), 93–107.
Kallmeyer, A.R., Krgo, A., Kurath, P., 2002. Evaluation of Multiaxial Fatigue Life Prediction Methodologies for Ti-6Al-4V. J. Eng. Mater. Technol. 124 (2), 229–237.
Madhi, E., Fretting fatigue behavior of nickel alloy IN-100. 2006.
Park, J., Nelson, D., 2000. Evaluation of an energy-based approach and a critical plane approach for predicting constant amplitude multiaxial fatigue life. Int. J. Fatigue 22 (1), 23–39.
Socie, D., 1987. Multiaxial Fatigue Damage Models.
Fuchs, H., Fatemi, A., Stephens, R., & Stephens, R. (2000). Metal Fatigue in Engineering 2nd Ed., ISBN 9780471510598. In: John Wiley & Sons Inc.
Murthy, H., Gao, G., Farris, T.N., 2006. Fretting fatigue of single crystal nickel at 600°C. Tribol. Int. 39 (10), 1227–1240.
Araújo, J.A., Nowell, D., 2002. The effect of rapidly varying contact stress fields on fretting fatigue. Int. J. Fatigue 24 (7), 763–775.
Infante-Garcia, D., et al., 2019. Numerical analysis of the influence of micro-voids on fretting fatigue crack initiation lifetime. Tribol. Int. 135, 121–129.
Navarro, C., Muñoz, S., Dominguez, J., 2008. On the use of multiaxial fatigue criteria for fretting fatigue life assessment. Int. J. Fatigue 30 (1), 32–44.
Navarro, C., Vázquez, J., Domínguez, J., 2017. Nucleation and early crack path in fretting fatigue. Int. J. Fatigue 100, 602–610.
Bhatti, N.A., Pereira, K., Abdel Wahab, M., 2018. A continuum damage mechanics approach for fretting fatigue under out of phase loading. Tribol. Int. 117, 39–51.
Shu, Y., Yang, G., Liu, Z., Hu, W., 2024. A comparative study of several life prediction models based on the critical plane approach for fretting fatigue crack initiation. Fatigue & Fracture of Engineering Materials & Structures 47 (5), 1495–1513.
Engineering Properties of In-100 Alloy. International Nickel; n.d.
Wang, C., Li, L., Zinovev, A., Terentyev, D., Wang, D., Wahab, M.A., 2023. Estimation of fretting fatigue lifetime in heterogeneous material based on microstructure characterization and multi-scale homogenization. Theor. Appl. Fract. Mech. 126, 103949.